

Wide-field mid-infrared cavity-enhanced upconversion imaging

Yue Song,^a Jia'nan Fang,^{a,b,*} Wen Zhang,^a Yijing Li,^a Ben Sun,^a Zhiwei Jia,^c Kun Huang^{b,d,e,*} and Heping Zeng^{b,a,b,e,f}

^aEast China Normal University, State Key Laboratory of Precision Spectroscopy, and Hainan Institute, Shanghai, China

^bChongqing Institute of East China Normal University, Chongqing Key Laboratory of Precision Optics, Chongqing, China

^cChinese Academy of Sciences, Institute of Semiconductors, Laboratory of Solid-State Optoelectronics Information Technology, Beijing, China

^dShanxi University, Collaborative Innovation Center of Extreme Optics, Taiyuan, China

^eShanghai Research Center for Quantum Sciences, Shanghai, China

^fChongqing Institute for Brain and Intelligence, Guangyang Bay Laboratory, Chongqing, China

Abstract. Mid-infrared (MIR) spectral imaging enables precise target identification and analysis by capturing rich chemical fingerprints, which calls for high-sensitivity broadband MIR imagers at room temperature. Here, we devise and implement a continuous-wave pumping MIR upconversion imaging system based on external-cavity enhancement, which favors a large field of view, a low cavity loss, and a high spectral resolution. The involved optical cavity is constructed in an integrated fashion by utilizing one crystal facet as a cavity mirror, which allows a 43-fold power enhancement for the single-longitudinal-mode pump at 1064 nm. In combination with the chirped-poling crystal design, high-fidelity and wide-field spectral imaging mapping is permitted to facilitate an acceptance angle of up to 28.5 deg over a spectral coverage of 2.5 to 5 μm . Moreover, a thermal locking approach is used to stabilize the cavity at high-power operation, eliminating active feedback and ensuring long-term stability. A proof-of-principle demonstration is presented to showcase real-time observation of CO₂ gas injection dynamics. The implemented MIR upconversion imager features wide-field operation, high detection sensitivity, and compact footprint, which would benefit subsequent applications, including environment monitoring, gas leakage inspection, and medical diagnostics.

Keywords: mid-infrared imaging; upconversion imaging; infrared detection; cavity enhancement.

Received Apr. 23, 2025; revised manuscript received Jun. 11, 2025; accepted for publication Jul. 14, 2025; published online Aug. 7, 2025.

© The Authors. Published by SPIE and CLP under a Creative Commons Attribution 4.0 International License. Distribution or reproduction of this work in whole or in part requires full attribution of the original publication, including its DOI.

[DOI: [10.1117/1.APN.4.5.056003](https://doi.org/10.1117/1.APN.4.5.056003)]

1 Introduction

Mid-infrared (MIR) spectrum covers vibrational–rotational transitions of molecules, thereby serving as the fingerprint spectral window for substance identification and analysis. Particularly, the chemical specificity renders MIR imaging useful in greenhouse gas monitoring and biomedical diagnostics.¹ With the urgent demand to mitigate issues of global warming and air pollution,² there is growing interest in accurate monitoring and mitigation of greenhouse gases such as CO₂ (at 4.3 μm), N₂O (at 4.5 μm), and CH₄ (at 3.3 μm), as well as harmful environmental pollutants.³ Monitoring these trace gases provides

critical data-driven insights for climate research, carbon emission tracking, industrial leak detection, and agricultural emission analysis. Moreover, MIR spectral imaging offers a noninvasive diagnostic tool for breath analysis.⁴ For instance, monitoring CO (at 4.6 μm) levels in exhaled human breath can reveal smoking-related pulmonary disorders⁵ or reflect heme oxygenase activity.⁶ Similarly, HCHO (at 3.6 μm) concentrations in breath correlate with tumor metabolism,⁷ providing a direct link to lung cancer and chronic inflammatory diseases. Typically, the aforementioned applications require gas detection sensitivities ranging from ppm to ppt levels, necessitating ultra-sensitive broadband MIR detection.

However, MIR detectors are typically achieved using narrow-bandgap semiconductor materials (e.g., HgCdTe, InSb, or PbSe),⁸ which suffer from high dark current noise at room

*Address all correspondence to Jianan Fang, jnfang@lps.ecnu.edu.cn; Kun Huang, khuang@lps.ecnu.edu.cn

temperature. Consequently, stringent cryogenic operation is usually required to enhance the detection sensitivity. For instance, cryogenically cooled HgCdTe avalanche photodiode arrays permit MIR single-photon detection,⁹ albeit with a limited pixel number. Recent advances in superconducting nanowire single-photon detectors have demonstrated impressively broadband responses in far-infrared wavelengths.^{10–12} Notably, the development of sensitive MIR sensors at room temperature has been fueled by emerging platforms based on low-dimensional materials^{13–16} or novel nanophotonic structures.^{17,18} In combination with high-brightness and wavelength-tunable quantum cascade lasers (QCLs), these MIR detectors enable direct acquisition of target-specific spectral image information with exceptional accuracy,^{19–21} although practical deployment still faces challenges in detection sensitivity, pixel scalability, and frame rates.

Alternatively, frequency upconversion imaging serves as an indirect yet effective approach to achieve ultra-sensitive MIR detection at the single-photon level.^{22–24} This method leverages nonlinear processes to transduce MIR information into the visible or near-infrared regime for accessing high-performance optical manipulation and detection.^{25,26} Recent advances in the pulse-pumped upconversion scheme favor high conversion efficiency due to the intensive peak power, which facilitates single-photon 3D imaging,^{27,28} high-speed hyperspectral imaging,^{29–31} and edge-enhanced imaging.^{32,33} However, such an active imaging modality typically requires tight synchronization and precise overlap with the ultrashort illumination source, which impedes efficient detection for temporally dispersed signals or randomly emitting fluorescences. Moreover, the intrinsic broadband nature of ultrashort pump pulses inevitably degrades the spectral conversion fidelity, thus limiting the resolution in spectroscopic applications.

In this context, continuous-wave (CW) pumping is proposed to realize high-resolution MIR spectral imaging.³⁴ One challenge for the passive scheme is to provide high pump power, especially for the single-pass configuration.³⁵ Although photonic waveguides can significantly enhance the intensity due to the tight mode confinement and long interaction length,^{36,37} the single-spatial-mode operation fundamentally precludes the wide-field imaging capability. One possible remedy is to resort to cavity enhancement techniques, where the nonlinear crystal is directly placed inside the laser resonator to implement intracavity power enhancement.^{38,39} This configuration facilitates an intracavity pump power up to ~ 100 W, leading to demonstrations of MIR photon-counting lidar^{40,41} and single-photon spectral imaging.⁴² However, the spectral proximity between the laser pump and the upconverted signal makes it difficult to suppress background noises via spectral filtering.⁴³ By contrast, the so-called external-cavity enhancement scheme spatially separates the pump source from the optical cavity, favoring noise suppression and system flexibility.^{44–46} Moreover, the configuration could benefit from the existing single-frequency lasers,⁴⁷ which enable high-resolution spectral measurements. Therefore, it is desirable to adopt the external-cavity scheme to realize high-efficiency and low-noise MIR upconversion imaging.

Here, we have proposed and implemented an external-cavity-enhanced MIR upconversion imaging system for the first time, which features high detection sensitivity, wide field of view (FOV), and broadband spectral coverage. The use of a

chirped-poling nonlinear crystal enabled an unprecedented acceptance angle up to 28.5 deg, over a wide-ranging operation wavelength from 2.5 to 5 μm . The optical cavity is specially designed using the crystal facet as one mirror, which favors a reduced optical loss and a more compact layout. The resulting finesse is optimized to 149, corresponding to a power enhancement factor of 43. Moreover, a thermal locking mechanism has been investigated to ensure long-term stability, eliminating the need for active feedback. In addition, we demonstrated video-rate wide-field MIR imaging of dynamic CO₂ jets, paving the way toward spectroscopic applications.

2 Experimental Setup

Figure 1 illustrates the experimental setup for the cavity-enhanced MIR upconversion imaging system. The pump source is from a Yb-doped fiber laser (YDFL) at 1064 nm. The YDFL is designed to stably operate at the single-frequency regime without suffering from the mode-hopping effect,⁴⁷ and its linewidth is <3 kHz. The YDFL delivers CW linearly polarized light at an average power of 39 mW, which is then boosted to 1 W using Yb-doped fiber amplifier (YDFA). To avoid back-reflection disturbance on the YDFL, a fiber optical isolator is employed. Subsequently, the pump beam is collimated using an aspheric lens. By rotating half-wave and quarter-wave plates, the pump's polarization can be finely tuned. The output of YDFA is coupled into the optical cavity, enabling subsequent pump power enhancement. Mode matching to the external cavity is achieved by optimizing both the fiber-to-lens distance and the collimator-to-cavity spacing.⁴⁴ The cavity finesse \mathcal{F} is evaluated to be ~ 149 from the ratio between the free spectral range and the cavity bandwidth.

Meanwhile, the MIR source is generated by a QCL and can be tuned from 4301 to 4310 nm by controlling the injection current. The maximum output power is 66 mW. The MIR light is collected into a single-mode fluoride fiber (P3-32F-FC-1, Thorlabs, Newton, New Jersey, United States) with a coupling efficiency of 56.5%, which allows easy light delivery and spatial mode cleaning. Then, the MIR beam is expanded to a 1-in. (1 in. = 2.54 cm) diameter using a pair of CaF₂ lenses L1 and L2. Moreover, the MIR beam is modulated by a spinning diffuser before illuminating the object to investigate the effect of spatial coherence on the imaging performance.

The MIR signal is sent into an upconversion $4f$ imaging system, where a chirped-poling lithium niobate (CPLN) crystal of 3 mm \times 2 mm \times 10 mm (width \times thickness \times length) is placed at the Fourier plane to perform sum-frequency generation. The focal lengths of two relay lenses (L3 and L4) are 50 and 100 mm, respectively. The CPLN is fabricated with linearly ramping poling periods from 16 to 24 μm . The resulting enlarged phase-matching acceptance angle leads to a wider FOV than that for single-poling crystals.²⁵ The upconverted light at 853 nm is steered through a spectral filter group (FG) consisting of a notch filter at 1064 nm, a long-pass filter with a cut-off wavelength of 700 nm, and a short-pass filter at 900 nm. The total transmission efficiency of the FG is $\sim 90\%$ with a rejection ratio for the pump of ~ 140 dB. Finally, the upconverted image is recorded by an electron multiplying charge-coupled device (EMCCD). Notably, the implemented upconverter is intrinsically broadband with a spectral coverage of 2.5 to 5 μm .

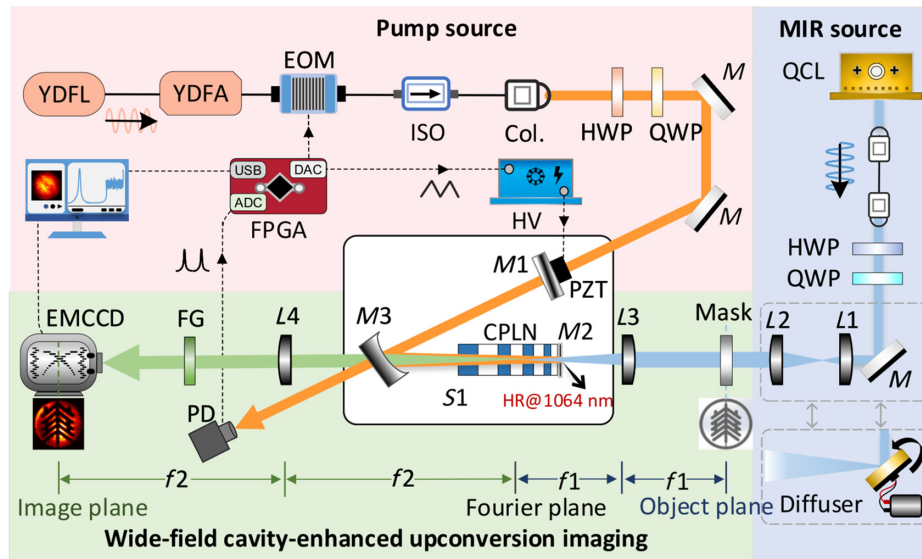


Fig. 1 Experimental setup of MIR upconversion imaging based on the external-cavity pumping. The pump source from a YDFL operates at the single-longitudinal mode at 1064 nm. The QCL serves as the MIR signal at a tunable wavelength around 4.3 μm . Then, the CW MIR beam is expanded with a pair of lenses before being steered into an optical cavity to implement the sum-frequency generation. The cavity is comprised of a flat mirror M1, a concave mirror M3, and a CPLN crystal. One crystal facet is coated with high reflection at 1.064 μm , thus serving as the end mirror. This cavity is stabilized with a digital locking unit based on a programmed field programmable gate array (FPGA). Under the locked state, the pump power can be significantly enhanced. The MIR signal after transmitting the object is then steered into a $4f$ imaging system, where the crystal is placed at the Fourier plane. The upconverted image is recorded by an EMCCD after passing through a series of spectral filters. YDFL and YDFA, Yb-doped fiber laser and Yb-doped fiber amplifier; EOM, electro-optical modulator; L, lens; M, mirror; Col., collimator; ISO, isolator; PZT, piezoelectric actuator; PD, photodiode; HV, high-voltage amplifier; FG, spectral filter group.

3 Results and Discussion

3.1 Design of Semi-monolithic Optical Cavity

In the following, we begin by presenting the design and characterization of the optical cavity. Figure 2(a) gives the schematic diagram of the implemented cavity, consisting of a flat mirror (M1), a CPLN with a reflective coating on one end (M2), and a concave mirror (M3) with a curvature of 200 mm. The power reflection at 1064 nm of these three cavity mirrors is 96.87% (M1), 99.9% (M2), and 99.95% (M3). Mirrors M1 and M3 are made of N-BK7. The coated crystal facet serves as one cavity mirror, enabling both a lower cavity loss and improved integrability. Such a monolithic cavity design is a good compromise between aligning flexibility and system stability. The CPLN crystal is mounted in a brass holder and secured on an aluminum plate. These materials favor a superior thermal conductivity, thus facilitating the heat dissipation to improve the thermal equilibrium. The CPLN crystal operates at room temperature without the need for precise temperature control to satisfy the phase-matching condition. Notably, M1 is mounted with a donut-shaped piezoelectric actuator (PZT, Thorlabs PA44M3KW), which offers an injecting port for the pump. The leaking light through M3 is detected by a photodiode, serving as the monitoring port for the cavity resonance. Finally, the entire optical external cavity is integrated onto an aluminum block with geometrical dimensions of 250 mm \times 135 mm \times 105 mm.

The cavity-mode size can be precisely controlled by tuning the mirror separations, yielding a 535- μm waist diameter at $D1 = 8.5$ cm and $D2 = 2.5$ cm, as shown in Fig. 2(b). This optimized beam size ensures a high pump intensity and a high spatial resolution for the subsequent upconversion imaging. The resulting Rayleigh length for the Gaussian mode is sufficiently long to avoid the crystal insertion loss. Figure 2(c) presents the beam-size evolution along the optical cavity. For a crystal thickness of 2 mm, the beam can propagate through the nonlinear crystal without suffering from beam truncation. Thanks to the spatial mode filtering for the pump, a nearly perfect mode matching is achieved with negligible high-order peaks. The presence of only the fundamental mode facilitates the cavity locking at a stable transverse mode. To ensure a stable cavity resonance at high-power operation, a thermal locking technique is proposed and implemented. The power in the cavity increases linearly with the power of the pump seed, as shown in Fig. 2(d). The power enhancement factor is deduced to be 50 from the line slope, favoring the access to high pump intensity with modest seed powers. When the cavity power exceeds 20 W, significant thermal expansion and lensing effects in the nonlinear crystal degrade spatial mode matching and introduce additional cavity losses, thereby reducing the finesse. As a result, in the presence of an input pump power of 0.7 W, the system achieves an intracavity power of 30 W, which enables a conversion efficiency of 0.1%. Note that the achieved modest efficiency is a common compromise for broadband upconversion imagers^{29,48} and favors

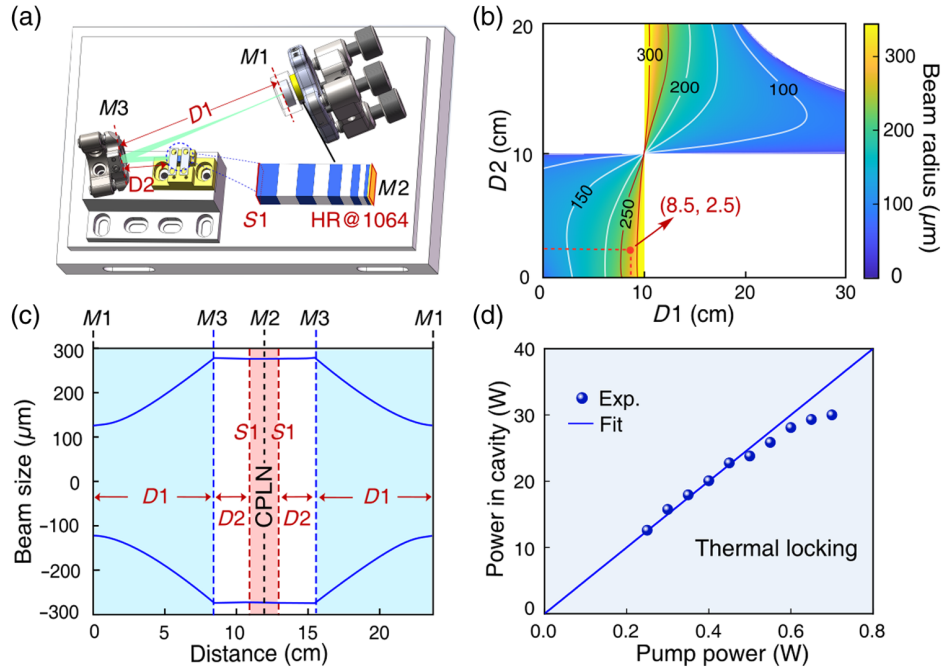


Fig. 2 Optical cavity design and characterization. (a) Diagram of the semi-monolithic optical cavity. The cavity consists of a mirror M1, a concave mirror M3, and a crystal end M2. The end of the crystal is coated with high reflection at $1.064 \mu\text{m}$, which is used as a flat mirror for the cavity. (b) Beam radius within the nonlinear crystal as a function of the distances of $D1$ and $D2$. The red point denotes the beam waist used in the experiment. Note that the white area represents the unstable region for an optical cavity. (c) Evolution of the beam waist along the optical cavity, when M1 is defined as the starting position. The shaded red area denotes the nonlinear crystal. (d) The intracavity power varies with the injected pump power. The thermal locking technique is used to stabilize the optical cavity at high-power operation.

a much lower injection pump power compared with the single-pass configuration.³⁵

3.2 Thermal Locking for Cavity Stabilization

Next, we further analyze the enhancement performance under thermal effects, which are manifested by shifts in transmission peaks when applying a high-voltage sawtooth waveform to the PZT for cavity-length sweeping. Figure 3(a) presents the behavior in the case of various injecting pump powers. The scanning rate is fixed at 20 Hz. As the pump power increases from 0.3 to 0.7 W, the asymmetry in the transmission peaks corresponding to the up- and down-scanning directions becomes more pronounced. Specifically, the up-scanning peak broadens, whereas the down-scanning peak becomes narrower. The underlying mechanism lies in the power-dependent length elongation due to the thermal expansion. When a higher voltage is applied to the PZT, the cavity length decreases [see Fig. 2(a)]. As the cavity approaches the resonance position, the intra-cavity power increases significantly. In response, the effective optical-path length of the crystal extends to compensate for the cavity-length reduction induced by the PZT. As a result, the resonating position is delayed relative to the “normal” one. Meanwhile, the peak looks spread during its positive slope, corresponding to a “slower scan.” In the down-scanning case, the cavity length extends as the voltage decreases. Consequently, the thermal-induced elongation accelerates the arrival at the resonance, thus resulting in a “faster scan” with a narrower peak width. Such

phenomenon would be more evident for a slower scanning speed due to the longer time to heat the crystal. Figure 3(b) presents the experimental observations at various scanning rates for a fixed injection power of 0.7 W. At a slower scan rate of 10 Hz, sufficient time is available for thermal accumulation, leading to a pronounced extension of the crystal’s optical path. This results in a significant delay of the cavity resonance during the up-scan. By contrast, at a higher scan rate of 50 Hz, the thermal effect is mitigated due to the relatively long relaxation time, thereby reducing the distortion of the transmission peaks.

To elucidate this phenomenon, a numerical simulation is performed to reveal the cavity dynamics in the presence of the thermal effect. Assuming the Fabry–Pérot cavity is impedance matched and lossless, the transmission power P_{trans} is given by⁴⁹

$$\frac{P_{\text{trans}}}{P_0} = \frac{1}{1 + \mathcal{F} \cdot \sin^2(kd)}, \quad (1)$$

where \mathcal{F} is the cavity finesse, P_0 denotes the optical cavity input power, k is the wave vector, and d is the optical length of the cavity. When accounting for thermal-expansion-induced path length variations, the phase kd depends on the temperature of the cavity. It can be expressed as $kd = w_0(d_0 + vt)[1 + \beta\Delta T(t)]/c$, where w_0 is the frequency of the light, c is the speed of light, d_0 denotes the initial cavity length at ambient temperature, $v = dd/dt$ represents the cavity length sweep speed, and β is a coefficient accounting for both material

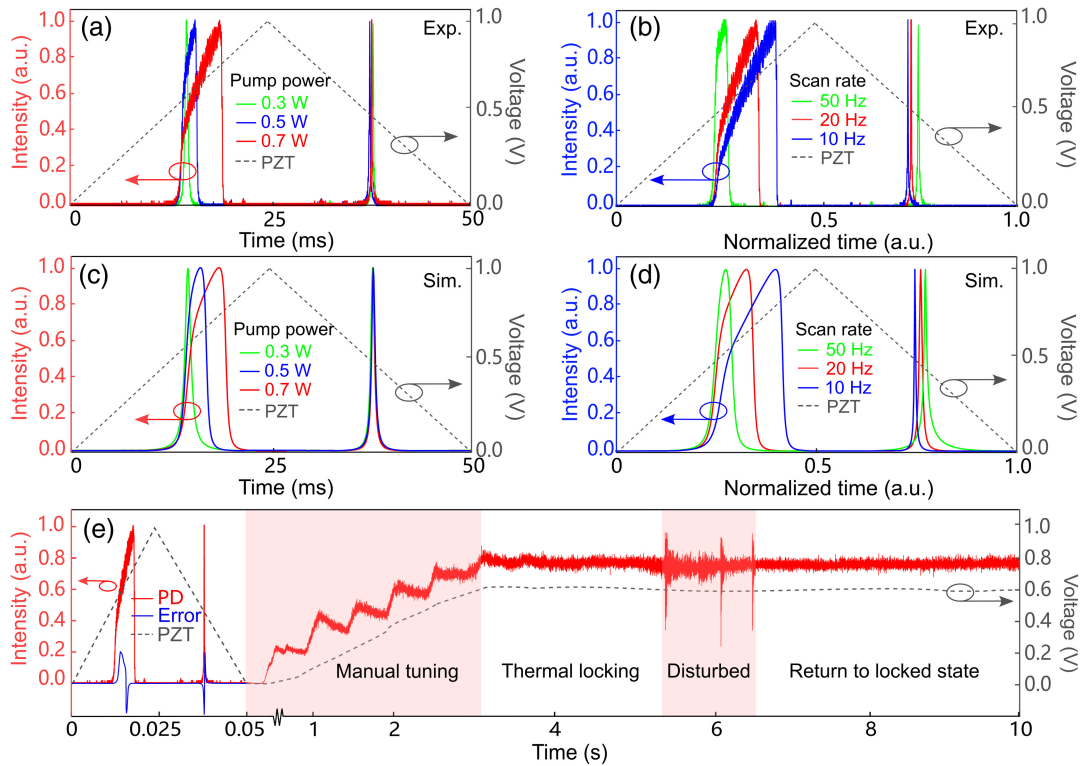


Fig. 3 Thermal effect on the crystal-embedded optical cavity. (a), (b) Experimental measurements of transmission peaks during the cavity-length scanning via the PZT in the case of various pump powers (a) and sweep rates (b). (c), (d) Corresponding numerical simulations at different pump powers (c) and sweep rates (d). (e) Process diagram of the optical locking based on the thermal effect. The locking operation initiates at 0.05 s and stabilizes after ~ 3 s. The signal vibration is due to the external disturbance for the purpose of verifying the robustness. Note that the behavior of the PDH locking is presented for the sake of direct comparison, which shows a pronounced thermal effect on the error signal.

thermal expansion and the change in refractive index with temperature. We assume the crystal's temperature response as a first-order impulse function $h(t)$ with a characteristic time constant τ_0 , i.e., $h(t) = (1/\tau_0) \exp(-t/\tau_0)$ when $t > 0$. Then $\Delta T(t) = \alpha P_{\text{trans}}(t) * h(t)$, where $P_{\text{trans}}(t) * h(t)$ represents the convolution of these two terms, and α is a positive constant. The simulation results for the transmission traces are plotted in Figs. 3(c) and 3(d) under different incident pump powers and scanning rates, which show good agreement with the measured responses.

Intriguingly, a passive thermal locking of the external optical cavity can be realized by leveraging the thermal effect, where the resulting broadening of the resonance peak effectively extends the range of cavity lengths that can sustain resonance. Specifically, thermal self-locking is accomplished by up-scanning the PZT and halting the scan just before the maximum intracavity power is reached, thus avoiding transition into the thermally unstable regime. Although the thermal locking confines the cavity operation to $\sim 85\%$ of the theoretical maximum power, it eliminates the need for complex active-feedback stabilization systems compared with previous works.⁴⁴ Figure 3(e) shows the intracavity power dynamics under thermal locking. The input pump power is set to 0.7 W, with a PZT scanning rate of 20 Hz. Asymmetry in the error signal in the conventional Pound–Drever–Hall (PDH) technique can be observed, thus

affecting the ability to stabilize the cavity precisely at the zero-crossing of the error signal. By manually tuning the high-voltage driver to initiate thermal locking, we can achieve a stable enhancement of the intracavity power. In the presence of repetitive mechanical shocks, the cavity returns to the locked state within a short time of ~ 0.1 s, demonstrating strong resilience against disturbances and robust self-recovery. Moreover, the chirped poling period design of the crystal enables a wide phase-matching bandwidth, which allows a larger tolerance for the heating-induced temperature variation. As a result, the conversion efficiency would be insensitive to thermal fluctuations while maintaining the locking stability of the optical cavity. Finally, long-term operational stability is achieved with optical power fluctuations of $\sim 2.5\%$.

3.3 Wide-Field Cavity-Enhanced Imaging

Now, we turn to investigate the performance of the MIR upconversion imager under both coherent and incoherent illumination conditions. A coherent MIR beam from the QCL is expanded to a 1-in. diameter and directed onto a USAF 1951 resolution target. The resulting upconverted image is shown in Fig. 4(a). Due to the aperture size of the input lens L3 in the $4f$ system, the FOV is constrained to ~ 1 in. in diameter. The smallest resolvable bars, indicated by dashed lines, correspond to element 1 in

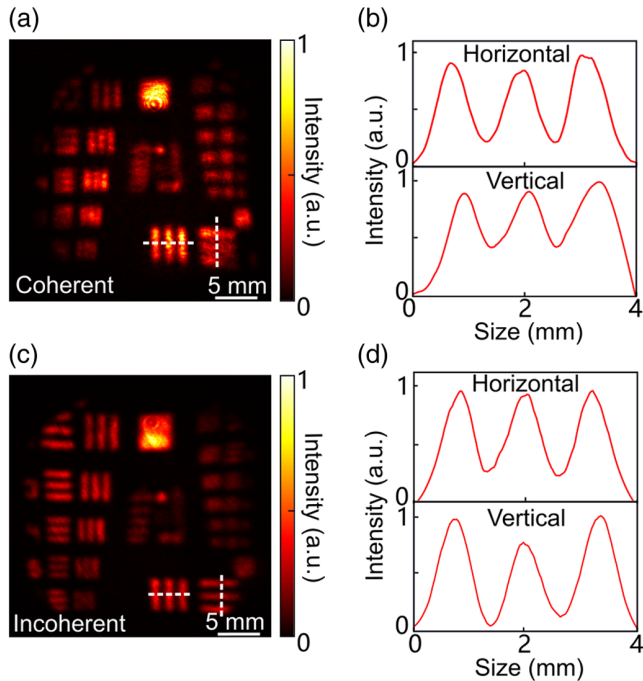


Fig. 4 Performance characterization of the MIR upconversion imaging under coherent and incoherent illuminations. (a) Coherent MIR upconversion images for the USAF resolution target. (b) Representative cross-section traces are given for the line pairs of the first element in the zeroth group under coherent illumination. (c) Incoherent MIR upconversion images. (d) Corresponding cross sections, which show an enhanced contrast. Note that all the images are acquired by an EMCCD at an exposure time of 80 ms.

group 0, with a spatial linewidth of $500 \mu\text{m}$. The corresponding intensity cross sections are displayed in Fig. 4(b), showing fringe contrasts of $\sim 58\%$ and 48% along the horizontal and vertical directions, respectively. The theoretical resolution limit of the system is given by $R = 4\lambda_s f_1 / \pi D_p$, where λ_s is the wavelength of the MIR signal, $f_1 = 50 \text{ mm}$ is the focal length of lens L3, and D_p is the pump beam waist within the nonlinear crystal. Increasing the pump beam waist enables the conversion of higher spatial-frequency components, thereby improving spatial resolution. However, a larger beam waist reduces the pump intensity, which in turn decreases the overall upconversion efficiency. To balance spatial resolution and detection sensitivity, the pump beam waist is optimized to $\sim 535 \mu\text{m}$. The corresponding theoretical resolution of $513 \mu\text{m}$ agrees well with the experimentally observed value.

For incoherent signals, the upconverted image corresponds to the convolution of the real-valued intensity distribution of the rescaled object with the intensity profile of the pump's Fourier transform. As this convolution is performed on intensity rather than field amplitude, the spatial resolution is theoretically improved by a factor of $\sqrt{2}$ compared with that in the coherent imaging regime. Experimentally, the MIR beam is modulated using a spinning diffuser prior to illuminating the object. This approach effectively suppresses speckle artifacts typically observed in coherent imaging due to the high spatial coherence of the laser source. To enable a direct comparison with the coherent case, the same resolution target is imaged under incoherent illumination. The resulting upconverted image is shown in

Fig. 4(c), revealing improved image uniformity and enhanced detail visibility. Cross-sectional intensity profiles are presented in Fig. 4(d), where the resolved bar width is measured to be $353 \mu\text{m}$, close to the theoretical prediction.

3.4 Real-Time Monitoring of Gas Flow Dynamics

Finally, we demonstrate the real-time CO_2 gas monitoring capability of the MIR imaging system. As shown in Fig. 5(a), CO_2 exhibits a strong absorption peak at 4308 nm . The narrow linewidth of the QCL enables precise spectral alignment with this feature, with the measured spectral width limited by the spectrometer's resolution ($\sim 0.1 \text{ nm}$). The experimental setup is illustrated in Fig. 5(b). The CO_2 is introduced into the imaging FOV under ambient conditions, with standard atmospheric pressure (1 atm) and room temperature (300 K). A sealed aluminum-foil gas bag filled with CO_2 serves as the source, connected to a fine-aperture nozzle for controlled injection into the FOV. The flow rate is precisely regulated using a needle valve to ensure consistent delivery and stable diffusion dynamics.

To better illustrate the CO_2 absorption process, we select a representative point along the gas flow path to monitor its MIR transmittance, as shown by the dynamic curve in Fig. 5(b). The transmittance exhibits temporal variations over a 4-s measurement window (see Video 1 for the corresponding real-time imaging sequence). At $T = 0.92 \text{ s}$, when the valve is closed, the CO_2 concentration within the FOV matches ambient levels, and the corresponding image intensity serves as the baseline reference for normalized transmittance. Upon gas release, the transmittance drops rapidly as CO_2 fills the monitored region. Figure 5(c) captures a full cycle of the CO_2 diffusion process between 2.28 and 2.44 s. The EMCCD camera operates at 25 frames per second (fps) (with a 40 ms exposure time per frame and a resolution of $1024 \text{ pixel} \times 1024 \text{ pixel}$). Notably, the system's high sensitivity permits even faster MIR imaging when equipped with high-speed CMOS detectors. The demonstrated combination of a wide FOV and high detection sensitivity underscores the system's potential for diverse applications, including environmental pollution monitoring, trace gas spectroscopy, and long-range target detection.

4 Conclusion

We have demonstrated an external-cavity-enhanced MIR upconversion imaging system, which features a wide FOV, a broad spectral coverage, and room-temperature operation. By applying anti-reflection coatings to the facets of the CPLN crystal in place of conventional cavity mirrors, we significantly reduced intracavity losses and improved the pump enhancement factor, resulting in a highly integrated cavity design. The decoupled configuration of the pump source and enhancement cavity enables the use of compact, single-frequency fiber lasers and amplifiers, thereby avoiding the spectral engineering challenges associated with solid-state lasers. This narrowband pumping scheme is particularly well suited for high-fidelity spectral mapping, making it highly attractive for precision molecular spectroscopy. Furthermore, the adoption of a thermal locking technique eliminates the need for complex active feedback systems while simultaneously increasing the tolerance to cavity-length variations and reducing the overall system footprint, hence beneficial for portable applications. In addition, the

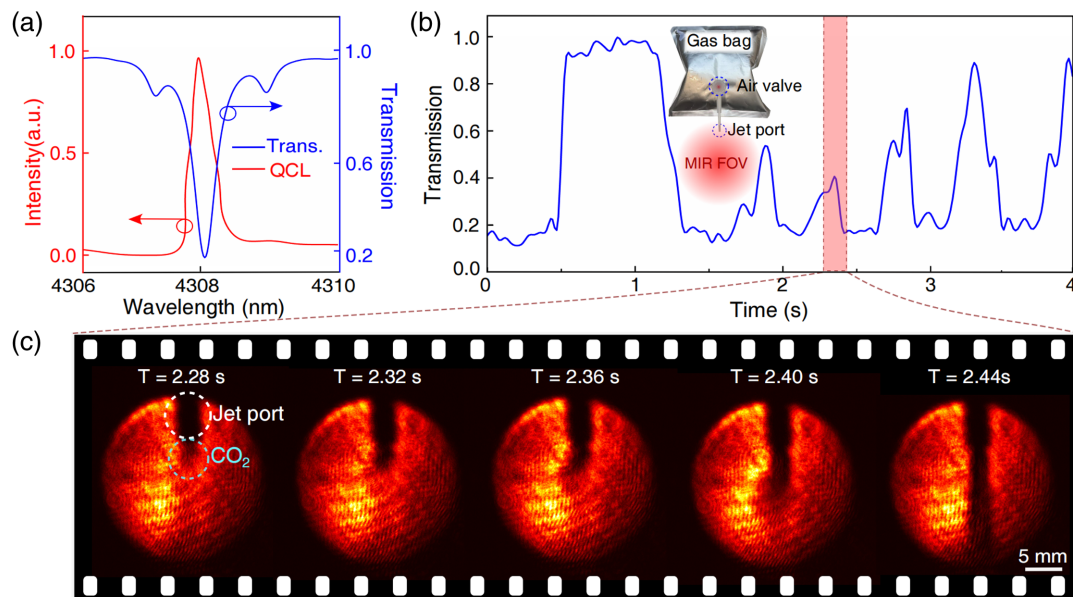


Fig. 5 Real-time MIR spectral imaging for gas flow monitoring. (a) Transmission spectrum of CO_2 at standard atmospheric pressure, which is obtained from the HITRAN database. The optical spectrum of the used QCL light source centers at 4308 nm, coinciding with the gas absorption peak. (b) Real-time monitoring of the CO_2 concentration within the imaging FOV. The CO_2 gas is delivered from a prefilled reservoir bag and injected into the imaging area through a nozzle, as illustrated in the inset. By repeatedly compressing the gas bag, the gas concentration varies in time as expected. (c) Spectral images during the period of 2.28 to 2.44 s. The MIR illumination power is $\sim 10 \mu\text{W}/\text{mm}^2$. The exposure time of the camera is set to 40 ms, corresponding to a frame rate of 25 fps. See [Video 1](#) for the recorded dynamics ([Video 1](#), MP4, 896 KB [URL: <https://doi.org/10.1117/1.APN.4.5.056003.s1>]).

system facilitates real-time gas flow monitoring, showcasing its robustness and potential for precision spectroscopic imaging. By integrating either a rapidly tunable broadband QCL/OPO source³¹ or a supercontinuum illuminator combined with fast spectral filtering of upconverted signals,³⁰ the system is well positioned for deployment in MIR hyperspectral imaging applications.

To go beyond the achieved performance, several avenues merit future investigation. First, the current spatial resolution is intrinsically limited by the Gaussian profile of the pump beam, which restricts the spatial frequency bandwidth in the Fourier plane. One promising approach is to engineer an optical cavity that supports elliptical pump resonances, thereby maximizing the utilization of the nonlinear crystal's cross-sectional area and enabling improved high-frequency component conversion through nonlinear Fourier ptychographic imaging.⁵⁰ Second, by applying high-reflectivity pump coatings to both end faces of the nonlinear crystal while introducing controlled curvature on one facet, the crystal can function as a plano-concave monolithic optical cavity. This architecture eliminates the need for external mirrors, leading to a compact, highly integrated design with reduced optical losses, making it well suited for broader deployment scenarios. In addition, the phase-matching condition in the nonlinear $4f$ imaging system induces wavelength-dependent radial shifts during the upconversion process, resulting in spatially dispersed broadband images.²⁹ This inherent dispersion provides a practical route toward snapshot MIR hyperspectral imaging.

Disclosures

The authors declare no competing interests.

Code and Data Availability

The data that support the findings of this study are available from the corresponding author upon reasonable request.

Acknowledgments

This work was supported by the Shanghai Pilot Program for Basic Research (Grant No. TQ20220104), the National Natural Science Foundation of China (Grant Nos. 62175064, 62235019, and 62035005), the Innovation Program for Quantum Science and Technology (Grant No. 2023ZD0301000), the Shanghai Municipal Science and Technology Major Project (Grant No. 2019SHZDZX01), the Natural Science Foundation of Chongqing (Grant Nos. CSTB2023NSCQ-JQX0011 and CSTB2022TIAD-DEX0036), the Fundamental Research Funds for the Central Universities, and the China Postdoctoral Science Foundation (Grant No. 2024M760918).

References

1. K. L. Vodopyanov, *Laser-Based Mid-Infrared Sources and Applications*, Wiley (2020).
2. A. A. Lacis et al., "Atmospheric CO_2 : principal control knob governing Earth's temperature," *Science* **330**, 356–359 (2014).

3. K. Santhanam and N. N. N. Ahamed, "Greenhouse gas sensors fabricated with new materials for monitoring climate change: a review," *J. Earth Sci. Clim. Change* **2**, 38 (2018).
4. K. Vjekoslav, *Handbook of Optoelectronics*, CRC Press (2018).
5. E. T. Middleton and A. H. Morice, "Breath carbon monoxide as an indication of smoking habit," *Chest* **117**, 758–763 (2000).
6. S. W. Ryter, "Carbon monoxide in exhaled breath testing and therapeutics," *J. Breath Res.* **7**, 017111 (2013).
7. A. T. Guntner et al., "E-nose sensing of low-ppb formaldehyde in gas mixtures at high relative humidity for breath screening of lung cancer," *ACS Sens.* **1**, 528–535 (2016).
8. M. Razeghi and B. M. Nguyen, "Advances in mid-infrared detection and imaging: a key issues review," *Rep. Prog. Phys.* **77**, 082401 (2014).
9. X. Sun et al., "HgCdTe avalanche photodiode array detectors with single photon sensitivity and integrated detector cooler assemblies for space LiDAR applications," *Opt. Eng.* **77**, 067103 (2019).
10. G. G. Taylor et al., "Low-noise single-photon counting superconducting nanowire detectors at infrared wavelengths up to 29 μm ," *Optica* **10**, 1672–1678 (2023).
11. Y. Pan et al., "Mid-infrared Nb₄N₃-based superconducting nanowire single photon detectors for wavelengths up to 10 μm ," *Opt. Express* **30**, 40044–40052 (2022).
12. Q. Chen et al., "Mid-infrared single photon detector with superconductor Mo_{0.8}Si_{0.2} nanowire," *Sci. Bull.* **66**, 965–968 (2021).
13. Y. Fang et al., "Mid-infrared photonics using 2D materials: status and challenges," *Laser Photonics Rev.* **14**, 1900098 (2020).
14. P. Wang et al., "Sensing infrared Photons at room temperature: from bulk materials to atomic layers," *Small* **15**, 1904396 (2019).
15. J. Wu et al., "Emerging low-dimensional materials for mid-infrared detection," *Nano Res.* **14**, 1863–1877 (2021).
16. X. Xue et al., "High-operating-temperature mid-infrared photodetectors via quantum dot gradient homojunction," *Light Sci. Appl.* **12**, 2 (2023).
17. A. Xomalis et al., "Detecting mid-infrared light by molecular frequency upconversion in dual-wavelength nanoantennas," *Science* **374**, 1268–1271 (2021).
18. W. Chen et al., "Continuous-wave frequency upconversion with a molecular optomechanical nanocavity," *Science* **374**, 1264–1267 (2021).
19. K. Haase et al., "Real time mid-infrared imaging of living microorganisms," *J. Biophotonics* **9**, 61–66 (2016).
20. L. Shi et al., "Mid-infrared metabolic imaging with vibrational probes," *Nat. Methods* **17**, 844–851 (2020).
21. Y. Kevin et al., "Fast infrared chemical imaging with a quantum cascade laser," *Anal. Chem.* **87**, 485–493 (2015).
22. A. Barh et al., "Parametric upconversion imaging and its applications," *Adv. Opt. Photonics* **11**, 952–1019 (2019).
23. K. Huang et al., "Mid-infrared photon counting and resolving via efficient frequency upconversion," *Photonics Res.* **9**, 259–265 (2021).
24. Y. Cai et al., "Mid-infrared single-photon upconversion spectroscopy enabled by nonlocal wavelength-to-time mapping," *Sci. Adv.* **10**, ead13503 (2024).
25. K. Huang et al., "Wide-field mid-infrared single-photon upconversion imaging," *Nat. Commun.* **13**, 1077 (2022).
26. S. Wolf et al., "Self-gated mid-infrared short pulse upconversion detection for gas sensing," *Opt. Express* **25**, 24459–24468 (2017).
27. J. Fang et al., "Mid-infrared single-photon 3D imaging," *Light Sci. Appl.* **12**, 144 (2023).
28. P. Rehai et al., "Noise-tolerant single photon sensitive three-dimensional imager," *Nat. Commun.* **11**, 921 (2020).
29. J. Fang et al., "Wide-field mid-infrared hyperspectral imaging beyond video rate," *Nat. Commun.* **15**, 1811 (2024).
30. Y. Zhao et al., "High-speed scanless entire bandwidth mid-infrared chemical imaging," *Nat. Commun.* **14**, 3929 (2023).
31. S. Junaid et al., "Video-rate, mid-infrared hyperspectral upconversion imaging," *Optica* **6**, 702–708 (2019).
32. Y. Wang et al., "Mid-infrared single-photon edge enhanced imaging based on nonlinear vortex filtering," *Laser Photonics Rev.* **15**, 2100189 (2021).
33. X. Zeng et al., "Tunable mid-infrared detail-enhanced imaging with micron-level spatial resolution and photon-number resolving sensitivity," *Laser Photonics Rev.* **17**, 2200446 (2023).
34. Q. Hu et al., "High-resolution mid-IR spectrometer based on frequency upconversion," *Opt. Lett.* **37**, 5232–5234 (2012).
35. Z. Ge et al., "Mid-infrared up-conversion imaging under different illumination conditions," *Phys. Rev. Appl.* **20**, 054060 (2023).
36. T. W. Neely et al., "Broadband mid-infrared frequency upconversion and spectroscopy with an aperiodically poled LiNbO₃ waveguide," *Opt. Lett.* **37**, 4332–4334 (2012).
37. K. D. F. Büchter et al., "All-optical Ti:PPLN wavelength conversion modules for free-space optical transmission links in the mid-infrared," *Opt. Lett.* **34**, 470–472 (2009).
38. M. F. Witinski, J. B. Paul, and J. G. Anderson, "Pump-enhanced difference-frequency generation at 3.3 μm ," *Appl. Opt.* **48**, 2600–2606 (2009).
39. K. Huang et al., "Observation of spectral mode splitting in a pump-enhanced ring cavity for mid-infrared generation," *Opt. Express* **27**, 11766–11775 (2019).
40. W. Yue et al., "Eye-safe aerosol and cloud Lidar based on free-space intracavity upconversion detection," *Remote Sens.* **14**, 2934 (2022).
41. M. Widarsson et al., "Room temperature photon-counting Lidar at 3 μm ," *Appl. Opt.* **61**, 884–889 (2022).
42. J. S. Dam, P. Tidemand-Lichtenberg, and C. Pedersen, "Room-temperature mid-infrared single-photon spectral imaging," *Nat. Photonics* **6**, 788–793 (2012).
43. R. L. Pedersen et al., "Characterization of the NEP of mid-infrared upconversion detectors," *IEEE Photonics Technol. Lett.* **31**, 681–684 (2019).
44. X. Liu et al., "Highly sensitive mid-infrared upconversion detection based on external-cavity pump enhancement," *Adv. Photonics Nexus* **3**, 046002 (2024).
45. M. A. Albota and N. C. W. Franco, "Efficient single-photon counting at 1.55 μm by means of frequency upconversion," *Opt. Lett.* **29**, 1449–1451 (2004).
46. S. Wolf et al., "Upconversion-enabled array spectrometer for the mid-infrared, featuring kilohertz spectra acquisition rates," *Opt. Express* **25**, 14504–14515 (2017).
47. S. Fu et al., "Review of recent progress on single-frequency fiber lasers," *J. Opt. Soc. Amer. B* **34**, A49–A62 (2017).
48. M. Mrejen et al., "Multicolor time-resolved upconversion imaging by adiabatic sum frequency conversion," *Laser Photonics Rev.* **14**, 2000040 (2020).
49. T. Carmon, L. Yang, and K. Vahala, "Dynamical thermal behavior and thermal self-stability of microcavities," *Opt. Express* **12**, 4742–4750, (2004).
50. T. Zheng et al., "Mid-infrared Fourier ptychographic upconversion imaging," *Optica* **11**, 1716–1724, (2024).

Biographies of the authors are not available.